Lab on a Chip

RSC Publishing

PAPER

View Article Online
View Journal

All-thermoplastic nanoplasmonic microfluidic device for transmission SPR biosensing†

Cite this: DOI: 10.1039/c2lc41123g

Lidija Malic,[a] Keith Morton,[a] Liviu Clime[a] and Teodor Veres*[ab]

Early and accurate disease diagnosis still remains a major challenge in clinical settings. Biomarkers could potentially provide useful tools for the detection and monitoring of disease progression, treatment safety and efficacy. Recent years have witnessed prodigious advancement in biosensor development with research directed towards rapid, real-time, label-free and sensitive biomarker detection. Among emerging techniques, nanoplasmonic biosensors pose tremendous potential to accelerate clinical diagnosis with real-time multiplexed analysis, rapid and miniaturized assays, low sample consumption and high sensitivity. In order to translate these technologies from the proof-of-principle concept level to point of care clinical diagnosis, integrated, portable devices having small footprint cartridges that house low-cost disposable consumables are sought. Towards this goal, we developed an all-polymeric nanoplasmonic microfluidic (NMF) transmission surface plasmon resonance (SPR) biosensor. The device was fabricated in thermoplastics using a simple, single step and cost-effective hot embossing technique amenable to mass production. The novel 3D hierarchical mold fabrication process enabled monolithic integration of blazed nanogratings within the detection chambers of a multichannel microfluidic system. Consequently, a single hard thermoplastic bottom substrate comprising plasmonic and fluidic features allowed integration of active fluidic elements, such as pneumatic valves, in the top soft thermoplastic cover, increasing device functionality. A simple and compact transmission-based optical setup was employed with multiplexed end-point or dual-channel kinetic detection capability which did not require stringent angular accuracy. The sensitivity, specificity and reproducibility of the transmission SPR biosensor was demonstrated through label-free immunodetection of soluble cell-surface glycoprotein sCD44 at clinically relevant picomolar to nanomolar concentrations.

Received 5th October 2012,
Accepted 22nd November 2012

DOI: 10.1039/c2lc41123g

www.rsc.org/loc

Introduction

Advances in genomic and proteomic investigations continues to generate new dimensions of possible disease-related targets.[1] For instance, CD44, a transmembrane glycoprotein expressed in many cell types, was recently demonstrated to play a significant role in tumor malignancy.[2] However, identification and characterization of targets, and in particular, different proteins, is often difficult and time consuming. Most of the available tools for early molecular detection, such as mass-spectrometers or antibody arrays,[3] are relatively expensive, require considerable expertise, and are not widely available. Therefore, a major challenge in medical diagnosis is the development of robust, portable and affordable assays.[4] Recently, biosensors have attracted a great deal of attention in this field which has led to many experimental and commercial systems with various optical, electrical or magnetic detection principles. In order to move biosensors to point-of-care (POC) diagnosis, important milestones need to be reached, including, among others, advances in sample preparation and integration with microfluidics, development of multi-channel biosensors, development of more sensitive and label-free transducers, compatibility with mass-manufacturing techniques and cost reduction.[5]

Plasmonic transducers have long been recognized for their potential to satisfy some of the above-mentioned requirements. As such, surface plasmon resonance (SPR)-based instruments are today one of the most popular class of biosensors due to their label-free, real-time detection, and high degree of automation and throughput. Conventional SPR sensors are constructed using the Kretschmann configuration where a gold-coated prism is used to resonantly couple incident light to collective electron oscillations, termed surface plasmons, propagating on the planar thin gold film. Most of these conventional prism-based SPR sensors require bulky and expensive optical equipment and, hence, are primarily used in a laboratory environment. It is noteworthy that significant

[a]National Research Council Canada, Boucherville, QC, Canada J4B 6Y4. Fax: +1(450)641-5105; Tel: +1(450)641-5232
[b]Biomedical Engineering Department, McGill University, Montreal, QC H3A 2B4, Canada

† Electronic supplementary information (ESI) available. See DOI: 10.1039/c2lc41123g

research efforts have been directed towards miniaturization and integration of SPR instrumentation.[6]

In concert with these developments, recent years have seen an increasing interest in plasmonic nanosensors which operate with small detection volumes and in the normal incidence condition, thus allowing simple, miniaturized instrumentation.[7] These exploit the localized surface plasmon resonances (LSPR) of noble metallic nanoparticles and surface-bound nanostructures having dimensions smaller than the wavelength of the interacting light.[8] Similarly to the SPR, the electric field of incident light collectively excites conduction band electrons to produce coherent localized plasmon oscillations. The ensuing strong electromagnetic field near the nanoparticle surface can be employed for surface-enhanced spectroscopic methods such as surface-enhanced Raman spectroscopy (SERS)[9–13] and enhanced SPR.[14–21] More importantly, the consequent strong extinction band (absorption and scattering) can be used as a chemical or biological molecular sensing platform.[22–25] In LSPR spectroscopy, the light extinction is heavily dependent on the nanoparticle's dielectric constant, size, geometry and interparticle spacing, and also on the dielectric constant of the surrounding medium. The latter allows the transduction of biomolecular binding events into a measurable wavelength shift of the extinction peak. Although the sensitivity of LSPR biosensors, with the added advantages of simple, portable and low-cost instrumentation,[26–28] has been shown to be comparable to traditional (propagating) SPR, the practical implementation of LSPR sensors could still benefit from improvements in reproducibility and monodispersity of the size and shape of the nanoparticles.[29]

A similar plasmonic response that is more stable and highly reproducible has been obtained with arrayed surface-bound metallic/dielectric nanostructures surrounded by planar gold film using SPR enhanced optical transmission (transmission SPR or T-SPR). Using visible light, such surface-bound nanostructures can be resonantly excited to produce surface plasmon oscillations consisting of either propagating or localized surface plasmons (SPPs or LSPs, respectively). In most cases, however, both SPP and LSP resonances are present and contribute to the optical characteristics of the nanostructure.[30] Nanostructures based on regular arrays of sub-wavelength nanoholes,[29,31–37] nanocavities,[38] nanoslits[39–43] or nanogratings[44–48] have been demonstrated in the T-SPR configuration. In comparison with other structures, nanogratings are particularly interesting as they represent an inherently information-rich substrate due to the ability to resonantly couple various diffracted orders to SPPs[49] under the momentum matching condition, as shown in eqn (1):

$$k_{sp} = \frac{2\pi}{\lambda_0}\mathrm{Re}\left\{\sqrt{\frac{\varepsilon_m\varepsilon_d}{\varepsilon_m+\varepsilon_d}}\right\} = \frac{2\pi}{\lambda_0}\sqrt{\varepsilon_d}\sin\theta_0 + m\frac{2\pi}{\Lambda} = k_{gm} \quad (1)$$

where k_{sp} is the real part of the propagation constant of SP, k_{gm} is the component of the wave vector of the diffracted wave parallel to the grating surface, λ_0 and θ_0 are the wavelength and angle of the incident p-polarized light (perpendicular to the grating grooves, TM), Λ is the grating period, ε_m is the metal's dielectric constant, and ε_d is the dielectric constant of the surrounding medium. Similar to other nanoplasmonic sensors, nanogratings also allow tuning of the plasmonic response by tailoring the shape, the amplitude, or the period of the grating profile.[46] Furthermore, their compatibility with mass fabrication makes nanogratings particularly attractive for fabrication of low-cost SPR sensing structures[50] and this is the approach taken in this paper. Moreover, emerging nanofabrication techniques provide the opportunity to integrate them with microfluidics for potential applications in POC medical diagnosis.

In addition to the low sample consumption allowed by miniaturization, microfluidic systems offer many benefits to nanoplasmonic sensors, such as excellent baseline stability, a high degree of control and automation and increased throughput. Also, microfluidic devices can significantly enhance mass transport to regions of the sensor surface, as diffusion lengths are minimized and convective transport replenishes the sample across the surface.[51] Though still in its infancy, microfluidic coupling with LSPR and T-SPR biosensors is an active area of research. Several groups have implemented single or multiple parallel microfluidic channels to precisely deliver low sample volumes to the nanostructured sensor surface.[52–55] For instance, simple flow cells sandwiched between a nanohole-based sensor substrate and a glass cover plate were reported,[56–57] as well as single[36,58] or multi-channel[59] PDMS or glass[60] microfluidic devices. More advanced multilayer PDMS devices with embedded nanohole perforated membranes as flow-through channels were also developed[31,61,62] in order to enhance the detection sensitivity. A multilayer device containing an array of flow channels controlled by a set of PDMS valves was recently demonstrated for early detection of a cancer biomarker using gold dimmers.[63] Finally, an elegant system integrating a nanohole T-SPR sensor with a 50-channel microfluidic network was developed for high throughput quantitative biomolecular binding studies.[35] Most of the reported microfluidic devices, however, were fabricated using PDMS soft lithography which is well adapted for small scale production required for proof-of-concept, but is not viable for commercial applications.

Currently, there is a need for new materials to be used for microfluidic nanoplasmonic biosensors that are mechanically robust, chemically inert, optically transparent and suitable for industrial-level production. Thermoplastics such as *Cyclo* Olefin Copolymer (COC) meet these requirements. While COC was previously demonstrated for the microfluidic part of an LSPR device,[64–66] the sensor chip comprised gold nanoparticles coated on a glass slide which increased the overall cost of the device and was difficult to bond and assemble against the hard COC microfluidic substrate.

In this paper we demonstrate the possibility to fabricate and monolithically integrate microfluidic channels with nanoplasmonic structures into COC substrates by nanoimprinting with a single 3D hierarchically structured mold. The fabricated nanoplasmonic microfluidic (NMF) biosensor has blazed nanograting structures embedded at the bottom of the

detection chambers, allowing easy integration with a control layer network of valves in the thermoplastic elastomer (TPE) cover for multiplexing. T-SPR was employed to characterize the biosensor response to bulk refractive index change and surface binding interactions. Experimental results were compared with numerical simulations to validate the observed asymmetries in the plasmonic response of the gratings. Lastly, we demonstrated the functionality of our system by specific and sensitive label-free immunodetection of soluble CD44 (sCD44) at clinically relevant concentrations.

Experimental section

Chemicals and reagents

Streptavidin (BioChemika), bovine serum albumin (BSA, $\geqslant$ 98%), phosphate buffer saline (PBS, pH 7.4), trichloro(1*H*,1*H*,2*H*,2*H*-perfluorooctyl)silane, dimethyl sulfoxide (DMSO) and ethanol were all purchased from Sigma-Aldrich (St. Louis, Mo, USA). HBS buffer (0.01 M HEPES, pH 7.4, 0.15 M NaCl, 3 mM EDTA, 0.005% Surfactant P20) was purchased from GE Healthcare. PEG-OH (hydroxy-terminated hexa(ethylene glycol) undecane thiol (OH)), PEG-COOH (carboxyl-terminated hexa(ethylene glycol) undecane thiol (COOH)) and PEG-Biotin (biotinylated tri(ethylene glycol) hexadecane thiol (Biotin)) were purchased from Nanoscience Instruments, USA. CD44 monoclonal antibodies (capture antibody cAb and detection antibody dAb) were purchased from Prospecbio, USA. Recombinant human CD44 antigen (MW $\sim$ 90 kDa) was purchased from R&D Systems, USA. All chemicals and reagents were used as received.

NMF biosensor device

The hybrid hard–soft polymeric NMF biosensor device (Fig. 1) employed for T-SPR measurements (Fig. 1c) is a multilayer structure consisting of a flow layer in a hard *cyclo*-olefin-copolymer (COC) thermoplastic substrate, a control layer in a soft styrenic ((styrene)–(ethylene/butylene)–(styrene) (SEBS) block copolymer) thermoplastic elastomer (TPE) and a thin TPE membrane sandwiched between the two (Fig. 1a). The flow layer comprised an 8 $\times$ 8 array of microfluidic detection chambers with monolithically integrated nanostructures covered by a 50 nm thick gold film (Fig. 1d). The nanostructures shown in Fig. 1d were composed of a polymeric nanograting array with sawtooth profile grooves (''blazed grating'', blaze angle $\theta_B \sim 27^\circ$). The 50 nm thick conformal gold layer exhibited a 4 nm wide groove (slit) at the grating apex (inset of Fig. 1e). Surface functionalization and sample loading into the detection chamber was achieved using a network of microchannels (the flow layer) controlled by an array of microvalves (the control layer). The device was operated using a pressure driven flow supplied by a multichannel syringe pump equipped with switching valves for buffer/sample loading (JKEM, USA). A custom built apparatus controlled by the Lab View program was used to supply pressure to the thin TPE membrane in order to close the valves and control fluid flow.

The device was used for both on-chip gold surface modification and sample delivery to the detection chambers. The reagents for surface functionalization were loaded into the reservoirs of eight functionalization channels and transported to the detection chambers by closing the valves of the sample loading channels. For proof of concept, a single surface chemistry was applied identically to all chambers; however, the device layout allows immobilization of eight different ligands using eight different reservoirs, as illustrated by the different channel colors in Fig. 1a. Following the gold surface functionalization, the valves on the functionalization channels were closed, and the sample was injected in each of the eight sample loading channels. This method allows potential investigation of up to 64 different surface binding interactions.

Fabrication

Polymer blazed nanograting fabrication

Grating structures were patterned by direct nanoimprint lithography of all-polymer substrates using UV-cured, soft-polymer working stamps as molds.[67] Rectangular profile silicon grating masters were made by electron beam lithography (NIL Technologies, Denmark) or deep UV lithography (LightSmyth Technologies, USA). Master gratings were then replicated by standard nanoimprint lithography (EVG520, EV Group) with spin-on resists (Nanonex 1020r, USA) and anisotropic RIE pattern transfer (Oxford Instruments, USA) in order to increase the grating aspect ratio of $\sim$2 : 1. These rectangular profile silicon gratings were then cleaned and treated with a fluorosilane mold release agent.

Polymer working stamp molds (Solvay MD700 with 1% Darocur 1173 photoinitiator) were then replica cast from the deeper silicon grating copies by UV-curing the liquid pre-polymer solution in contact with a supporting rigid glass backplane. Overall, the mold itself is rigid, supported by the glass backplane, but locally the replica-cast polymer grating ridges are flexible and can bend when imprinted. Pressed into a nanoimprint resist (Nanonex 1020r) spin coated onto silicon wafers, the intrinsic lateral shear forces in the parallel plate imprint press partially collapse the flexible grating structures to form a blazed grating profile in the imprint resist, as seen in the cross-sectional SEM image in Fig. 1e. The shorter blazed length corresponds to the top of the grating ridge, while the longer length corresponds to one side of the flexible grating ridge. The as-imprinted blazed polymer gratings form a new, quasi-3D nanostructured master for replica casting. This replica mold of the blazed grating, made using the UV-cured polymer working stamp material, was then repeatedly used to emboss (EVG520, EV Group) the sharp-cornered, blazed grating profile directly into COC (Zeonor^{TM}) wafers.

Microfluidic device fabrication

Flow layer. The NMF biosensor was fabricated using the procedure illustrated in Fig. S1a, ESI,† which for clarity shows a single chamber and none of the channels or other microfluidic features. A soft TPE membrane was hot-embossed to form microscale features (microchannels and chambers), including through-holes at the chamber location, using a procedure similar to the one previously developed by our

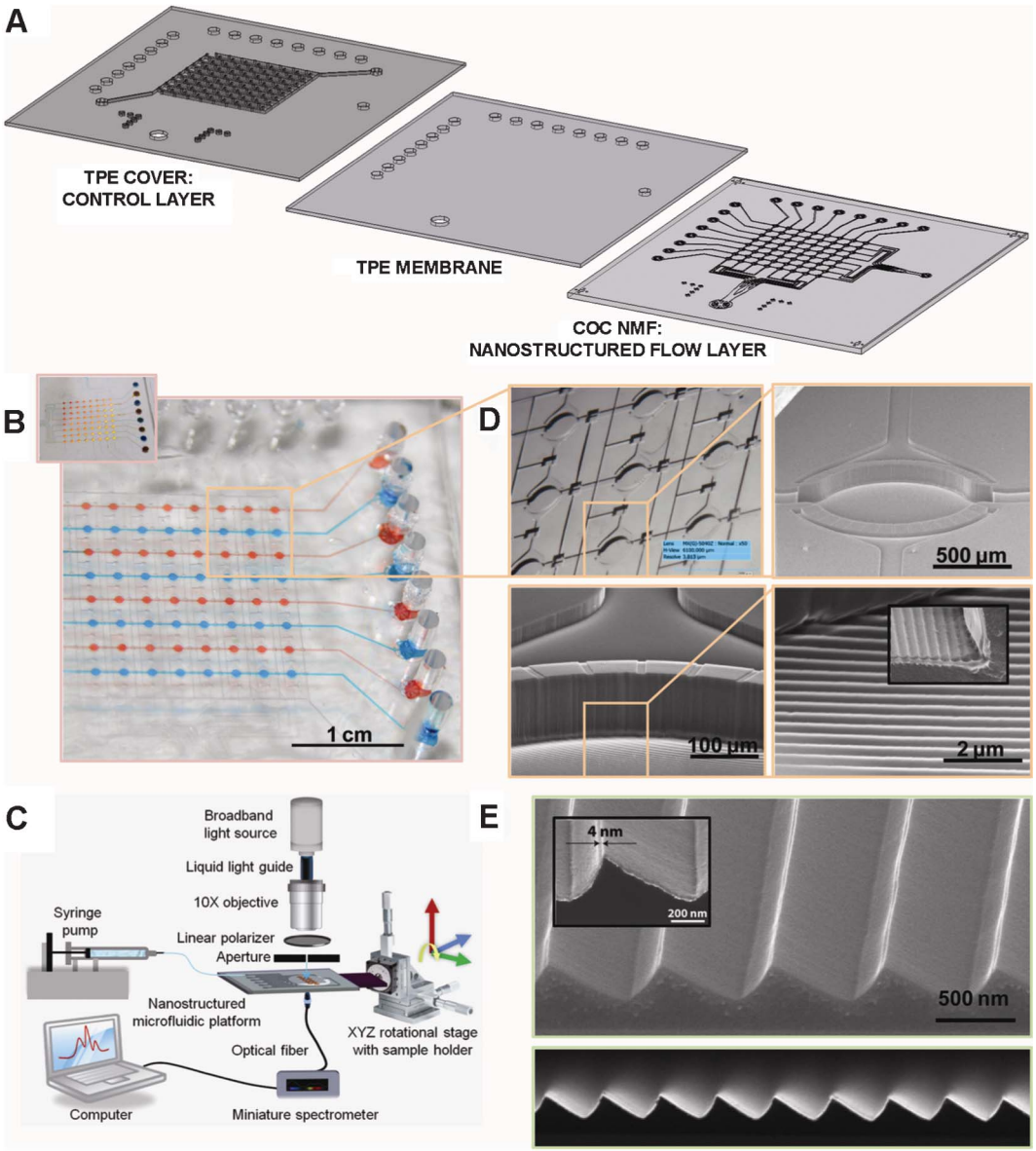

Fig. 1 Nanoplasmonic microfluidic (NMF) transmission-based SPR biosensor (a) Schematic illustrating multilayer device consisting of a top control layer in TPE, a middle membrane layer in TPE and a nanostructured flow layer in COC; (b) image of a NMF device with monolithically integrated nanogratings; (c) schematic illustrating the experimental setup used for measuring the transmission spectra through the detection chamber of the device; (d) 3D optical image and SEM micrographs showing the detection chamber and the monolithically integrated blazed nanograting structures on the bottom of the chambers; (e) SEM micrographs of 700 nm period blazed nanogratings covered with 50 nm gold. The inset shows a 4 nm wide groove residing on the tip of the triangular grating structure as a result of the gold deposition process on the COC grating.

group.[68] Briefly, a multilayer SU-8 mold, used to emboss a thin TPE membrane, was patterned using standard photolithography to form microchannels (5 µm and 25 µm deep) and detection chambers (100 µm deep). Subsequently, the embossing of the TPE membrane was performed at an applied pressure of 15 kN for 15 min at 140 °C (EVG520, EV Group). Separately, a hard Zeonor™ substrate was patterned by hot-embossing at an applied pressure of 20 kN for 5 min at 160 °C to form a regular array of nanograting elements (see Section 2.3.1).

Next, with the microchannel features facing up, the TPE membrane was placed on the Zeonor™ substrate such that the through-holes exposed the grating elements. In order to form the master mold, the soft flexible membrane was then reversibly bonded to the Zeonor™ substrate at room temperature by applying a pressure to seal the membrane around the through-holes against the Zeonor™ substrate. Photocurable polymer (Solvay MD700 with 1% Darocur 1173 photoinitiator) was then poured into the through-hole and onto the membrane to cover the membrane and the microchannels. A glass plate was placed over the top of the

photocurable polymer and cured for 5 min using UV radiation. After curing, the master mold and the glass plate were removed to provide a working stamp having reliefs comprising a reverse image of the microchannels, chambers and the regular array of nano-scale grating elements on the bottom of the detection chambers (Fig. S1b, ESI†).

The working stamp was then used to hot-emboss Zeonor substrate to provide, in one step, a monolithic nanostructured microfluidic device (Fig. 1d). Finally, selective metallization of the detection chamber regions was performed using a second TPE membrane mask with through-holes aligned with the detection chambers in order to avoid any further photolithography/etching steps. Metallization was conformal to the nanostructured gratings; typically 50 nm thick gold films were deposited by RF sputtering (Kurt Lesker) at room temperature with the substrate mounted on a rotating stage. No chromium adhesion layer was necessary as the as-deposited films passed tape peel-off tests. Due to the shadowing effect during deposition stage rotation,[69] a 4 nm wide groove (slit) was created in the gold film along the apex of the blazed grating structures.

Control layer. The control layer was fabricated using a process similar to our group's previously published procedures.[70] Briefly, an SU-8 mold containing control channels was fabricated using standard photolithography. The mold was subsequently treated with silane and used to emboss a TPE substrate for 20 min at 140 °C and an applied pressure of 10 kN. The same procedure was employed to obtain a 40 μm thin TPE membrane for pneumatically controlled valves by embossing a 100 μm thick TPE film with a mold comprising 60 μm deep SU-8 spacers.

Device assembly. Following the fabrication of the three layers, inlet holes were punched in the control and membrane layers and the device was assembled by first placing a thin TPE membrane on the Zeonor substrate. Next, the control layer was aligned and placed on the TPE membrane and irreversible bonding of the multilayer structure was achieved using a 3 min thermal treatment at 100 °C.

Numerical modeling

The well-established rigorous coupled-wave analysis (RCWA)[71,72] was employed to corroborate the nanograting size (θ_B = 27°; height = 240 nm), period (Λ = 700 nm), and the Au film thickness (t = 50 nm) to the experimental results, using a custom written routine implemented in Matlab (see Fig. S2, ESI;† based on GDCalc™). The simulation was performed by scanning the wavelength of incoming transverse magnetic (TM) polarized monochromatic plane waves at normal incidence with a spectral resolution of 0.08 nm. Calculations were carried out using 55 space harmonics with 1 nm resolution in the grating depth axis. The complex permittivity of gold was taken from ref. 82, while the refractive index used for the COC substrate and dielectric medium corresponded to 1.525 and 1.333, respectively.

Transmission SPR spectroscopy

A custom-built optical system shown in Fig. 1b was used to perform all optical transmission measurements in a collinear geometry. White light from a halogen source (model OSL1, Thorlabs, USA) was coupled to a 3 mm core diameter liquid light guide (model LLG0338-6, Thorlabs, USA) and collimated with a lens (PL FL 10x, Nikon, USA) prior to passing through a polarizer and illuminating the sample through the 1 mm pinhole of the same size as the detection chamber of the NMF device. The device was placed on the sample holder which consisted of a carrier manifold connected to a rotational stage in order to allow for spectral transmission measurements at specific angles of incidence. The rotational stage was further mounted on an XYZ stage in order to allow precise alignment of each chamber to the illumination beam for sequential spectral measurements. The light transmitted through the sample was collected by a 0.6 mm diameter optical fiber and recorded with a miniature spectrometer (model USB4000, Ocean Optics, USA). Each spectrum consisted of the average of 100 individual spectra which were further processed in MATLAB in order to quantify the peak/dip shift (resonant wavelength shift, $\Delta\lambda$). This was performed using Lorentzian curve fitting in the least square sense by minimizing the sum of squared residual differences between the fit curves (Lorentzian) and the experimental values. All the reported peak/dip shifts represent the average values taken over the eight chambers in the first row of the eight columns of the device.

Bulk refractive index sensing

In order to assess the sensitivity of the device to the bulk refractive index change, various index-calibrated water–glycerol solutions (from n = 1.333 to 1.398) were sequentially injected into the microfluidic device. Spectra for each solution were recorded using the T-SPR setup and the estimated device sensitivity was taken as the slope of the curve representing the linear fit of a resonance peak or dip shift ($\Delta\lambda$) per refractive index unit change (RIU). The corresponding figure of merit (FOM) was defined as the ratio of the sensitivity to the resonant width of the spectral peak (full width half maximum, FWHM), where the resonant width is measured at the midpoint of intensity corresponding to the difference between the intensity of the first peak (dip) and the neighboring dip (peak),[39,73] as shown in Fig. S3, ESI.†

Surface functionalization

On-chip gold surface functionalization was performed for all chambers in parallel. The flow rate for all solutions was kept at 5 μl min^{-1}. We used a slightly modified mixed monothiol procedure which was reported previously.[74] Briefly, for streptavidin binding studies, a 1 mM solution containing a 1 : 9 ratio of PEG-Biotin : PEG-OH in ethanol was injected continuously for 1 h to form a mixed SAM (self-assembled monolayer) on the surface. The surface was then rinsed in sequence with absolute ethanol and ultrapure water (18.2 mΩ cm). For capture antibody (cAb) immobilization, the gold-surface was modified with a 1 mM PEG-OH : PEG-COOH (1 : 4) mixture for 8 h, followed by an ethanol–water rinse. Next, a NHS–EDC (50 mM–200 mM) solution was injected for 30 min in order to activate amine groups. Finally, the surface was sequentially rinsed with ultrapure water and PBS buffer, followed by cAb immobilization for 3 h at a concentration of 50 μg mL^{-1} in PBS. After immobilization, the surface was

rinsed with PBS buffer, followed by deactivation of amine groups by injecting 50 mM ethanolamine for 30 min.

T-SPR immunoassay kinetic measurements

T-SPRi detection of biomolecular binding interactions was performed using the setup described in Section 2.4. In order to determine the resonant peak/dip that exhibits the maximum wavelength shift ($\Delta\lambda$) for surface binding reactions, the kinetics of streptavidin–biotin binding and cAb immobilization were recorded for each resonant peak. Subsequently, CD44 immunoassay kinetics were obtained sequentially for each detection chamber by monitoring the spectral shifts of the second transmission minimum around 690 nm, which provided the highest sensitivity at normal incidence. The kinetic curves were traced as a function of time, showing the kinetics of the binding events that take place at the surface of the chip. All solutions were introduced into the channels continuously at a flow rate of 5 μl min^{-1} and the reported curves were averaged over eight chambers. Sandwich immunoassay was performed using CD44 antigen and dAb in HBS buffer. A 5 min baseline signal was obtained first for the HBS buffer, followed by the antigen binding signal for which different CD44 concentrations were injected sequentially into each channel, allowing the antigen to bind to the immobilized cAb for 30 min. Following the protein binding, dAb was introduced at a concentration of 20 μg mL^{-1} in HBS buffer and flowed for 30 min. Finally, the substrate was washed with buffer for 5 min and the difference in the resonant wavelength shift was computed by taking the difference between the initial and final buffer signals. After measuring the immune response, the sensor chip was regenerated by injecting 50 mM NaOH–1 M NaCl for 5 min. To investigate non-specific binding, a control experiment was performed by injecting a 20 μg mL^{-1} concentration of BSA instead of CD44 over the immobilized surface. The reported limit of detection (LOD) represents the minimum detectable target concentration for which the signal is at least three times higher than that of the control.

Results and discussion

We have developed an integrated nanoplasmonic microfluidic (NMF) system in order to precisely control and detect biomolecular binding interactions using label-free T-SPR readings. The integrated system (Fig. 1) represents a monolithic microfluidic structure in a polymer substrate with embedded (polymer and metal) blazed nanogratings fabricated using a single 3D hierarchically structured mold.

Nanoplasmonic microfluidic device fabrication

A novel process was developed to allow the fabrication of molds for low-cost high-throughput production of monolithically integrated nanostructures within the microfluidic channels in thermoplastics. A single layer working stamp containing microfluidic channels, chambers, and nanostructures was fabricated from a multilayer polymeric master mold. The master mold was composed of a nanostructured hard COC substrate reversibly bonded to a microstructured soft TPE membrane with the microchannels facing up and through-holes exposing COC nanogratings (Experimental Section). Nanoimprinting was used to define both the microchannels in TPE and the nanostructures in the COC substrates. Direct nanostructuring of the optical quality, monolithic, polymer wafers eliminated the need for spin-on imprint resists, residual layer RIE etching or other downstream pattern transfer steps. The multilayer mold fabrication method separated the nanofabrication from microfabrication processes, overcoming the issues of material and reagent compatibility common in conventional procedures involving multiple lithography/etching steps. The resulting 3D hierarchically structured working stamp allowed embossing of NMF devices in a single step, thus eliminating topographical surface variations induced by sample-to-sample fabrication differences. As such, the integrity and reproducibility of the nanostructured substrate's plasmonic response between devices was preserved. The novel fabrication method thus allows highly reproducible device fabrication which can be easily scaled to industry-level production.[75] In addition, the developed low-cost and rapid mold fabrication technique allows interchangeable microfluidic device design for easy fluidic adaptation using identical nanostructures. In order to implement a different microchannel/reservoir layout, the soft TPE membrane can be simply delaminated from the COC substrate and replaced with a new design without compromising the nanoplasmonic sensor response. Finally, by integrating the nanoplasmonic sensor within the flow layer, the control channels can be more easily incorporated in the top cover, an essential feature required for multiplexing.

Refractive index sensing and bulk sensitivity characterization

Efficient coupling of incoming light to SPP waves is typically achieved using oblique incidence on a grating *via* phase matching of one evanescent diffraction order to an SPP mode. However, for integrated biosensors, normal incidence is preferable as it alleviates the need for added complexity in the optical system design required for angular control. Unfortunately, the coupling efficiency for normal incidence is typically low due to diffraction losses. To overcome this, it has been recently shown that asymmetrical excitation of SPPs on nanogratings at normal incidence can be achieved using asymmetrical slanted grating profiles.[76,77] When the asymmetry effect is large, even unidirectional SPP propagation can be achieved, an effect similar to that observed for backside illuminated grating–slit configuration.[78] However, the elaborate fabrication procedures required to produce asymmetrical grating profiles, such as direct laser-beam or ion-beam milling, single-beam holographic lithography, a series of photolithographic processes for staircase surface profile approximation or inclined-angle reactive-ion beam etching with a binary grating mask, increase the cost and the complexity of these devices, preventing their use in biosensing applications.[77] In this paper, a simple, cost-effective fabrication procedure has been developed to create a sawtooth grating profile in COC, uniformly coated with gold film that exhibits a nanoslit at the grating apex. The nanoplasmonic sensor was monolithically integrated with the microfluidic device and employed for efficient SPP coupling under normal

incidence. Fig. 2a and 2b show experimentally and numerically obtained spectrograms for both s- and p- polarizations (TE and TM, respectively) of blazed gratings at normal incidence. In both cases, the resonances were observed only when there was a component of the electric field of the incident radiation normal to the local grating surface (TM polarization), indicating coupling to surface plasmons.[79] The small differences between the experimentally obtained and numerically calculated resonance positions (peaks and dips) were attributed to the presence of the 4 nm narrow groove (nanoslit) at the blazed grating apex, a feature that was not included in the model. Since the electromagnetic field enhancement was highest at the tips of the sharp blazed grating (see inset of Fig. 2b), the presence of the nanogroove at this location caused an additional resonance shift, as observed in the experimental results. Optical SPP excitation on blazed gratings for incident light was also confirmed by comparing the grating spectrograms with those of the flat gold surface (control). From the inset of Fig. 2c, unlike the blazed gratings, the control exhibited an identical spectral profile for both polarizations (inset of Fig. 2c). Conversely, nanogratings enabled SPR-enhanced transmission under TM-polarization, as evidenced by the ratio of p- and s-polarized transmitted light intensities for values greater than 1 (*i.e.* $T_p/T_s > 1$).[44] The grating spectrum exhibited an asymmetric resonant profile having transmission peaks accompanied by dips (Fano-type resonance profile), such that the frequency of the SPP excitation does not correspond with either the transmission maximum or minimum, but rather lies somewhere in between.[80,81] This is a consequence of the incoming wave (continuum state) coupling with the surface-bound SPP of a periodic array (a discrete state) and the resulting interference between the narrow SPP and broad-band LSPR associated with gap plasmons in the nanoslit.[39] Therefore, from Fig. 2c, we can attribute the strong wavelength dependant modulations (maxima at 556, 637 and 724 nm and minima at 582 and 687 nm) to excitation and interaction of SPP and LSP modes. The multichannel resonance capability of the blazed gratings opens up the

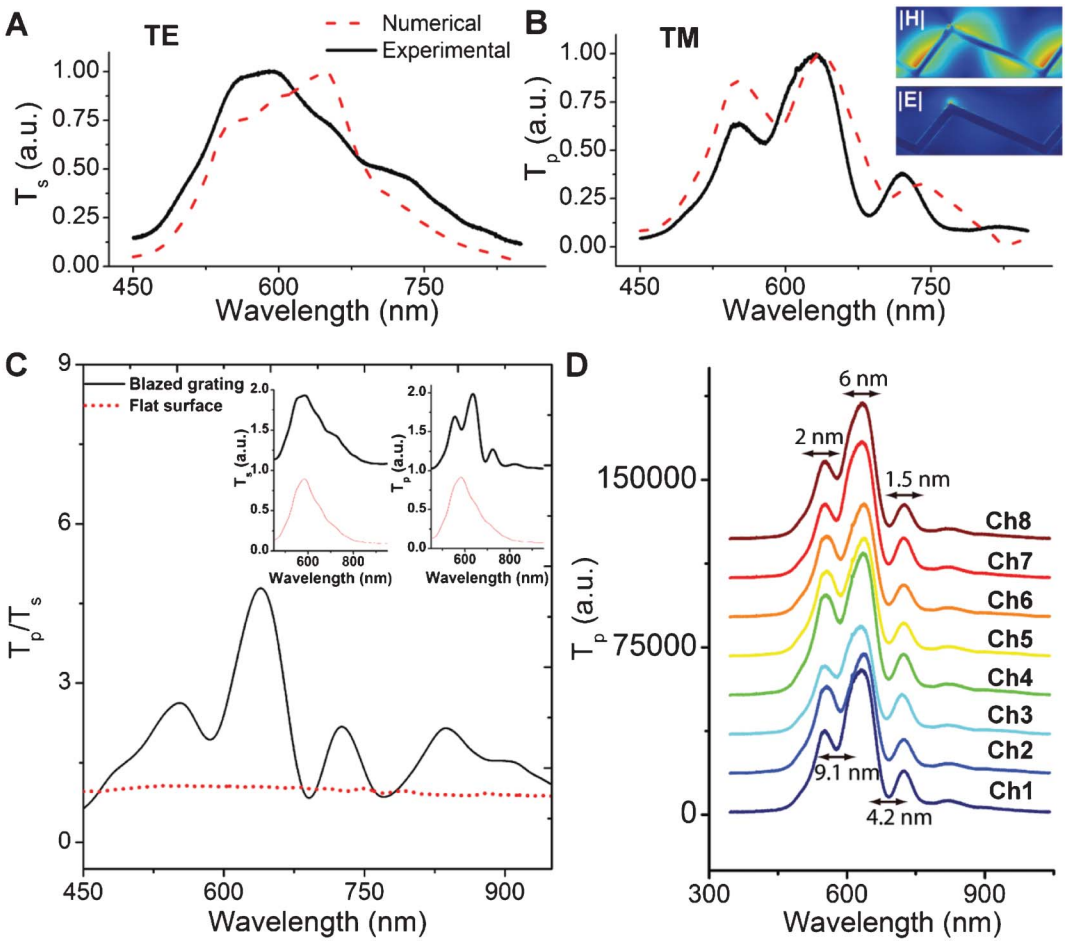

Fig. 2 (a) and (b) s- and p- polarizations of experimentally and numerically obtained transmitted light spectra for blazed grating. Inset shows the near field calculations of magnetic and electric field intensities, demonstrating the highest field enhancement at the grating apex. (c) Ratio of transmitted p-polarized to s-polarized light (T_p/T_s) for flat surface and blazed grating, showing regions where surface plasmon excitation occurs as the enhancement of this ratio over the nominal value of 1 for the blazed grating substrate. The inset shows transmission spectra at normal incidence for a 50 nm thick gold film on a flat surface and a blazed grating with s-polarized and p-polarized light. The curves have been normalized to 1 and offset for clarity. (d) Transmission spectra across the eight chambers of the first row of the device, showing the uniformity of the resonance maxima/minima positions. The numerical values for the spectral dispersion of each peak are included.

possibility to monitor and discriminate multiple binding interactions in parallel. Moreover, the existence of multiple transmission peaks and dips indicates that the blazed gratings can be used for SPR based sensing with light sources of different wavelengths corresponding to the maxima or minima in the transmission spectra. The resonance positioned at ~724 nm closely corresponds to the theoretical value of the first diffracted order coupling to SPP (as calculated by eq(1) for $m = 1$, $\Lambda = 0.7$ μm, $\varepsilon_d = 1.33$, and $\varepsilon_m = -20.61 + 1.27i$ for gold at 757 nm[82]), while the remaining two resonances seem to be a result of SPP–LSP interaction,[83] although it is not clear how much contribution comes from each. Because of this coupling between propagating SPPs and LSPR, the positions of transmission maxima/minima around 550 nm and 650 nm do not coincide with the resonances provided by the grating eqn (1).

Additionally, eqn (1) does not take into account the presence of the nanoslits, the associated scattering losses, and thus it neglects the interference that gives rise to additional resonance shifts.[84] From Fig. 2a, the Fano-type resonances at 556, 582, 637, 687, and 724 nm were characterized by fairly narrow bandwidths, with FWHM (Fig. S3, ESI†) corresponding to 16, 22, 27, 17, and 20 nm, respectively. This can allow easier determination of the spectral peak/dip positions in biosensor applications. For high-throughput applications, the uniformity of the large area nanostructure was also an important consideration. From Fig. 2d, quite uniform spectral peak positions were obtained across the device, as shown for the eight chambers in the first row of the chip (1 × 18 mm area) that were used for the interrogation of biomolecular binding reactions.

To estimate the sensitivity, and the corresponding figure of merit (FOM) of the nanograting structure, the resonant wavelength shift was measured as a function of the bulk refractive index change (Fig. 3). Different glycerin concentrations in water (0% to 50%) were flowed through the microfluidic channel network and the resonant wavelength shift was recorded as a difference between the glycerol solution and water taken as a control. We found a linear red-shift of the transmission maxima/minima as a function of the increasing effective index (see Fig. 3) which allowed us to calculate the bulk sensitivity. The maximum sensitivity was observed for the transmission minimum around 690 nm, with an estimated sensitivity of 230 nm/RIU and FOM of 12.8/RIU.

The sensitivity found in our experiments agrees well with the values predicted for grating-based SPR devices[47,85] and are similar to the sensitivities obtained from sensing schemes based on metallic nanoparticles.[28,86] The resonances occurring at longer wavelengths close to the NIR regions of the spectrum (lower energy) exhibited higher sensitivity, which is in agreement with previously published results.[87–89] In particular, the second minimum (D2) experienced the largest spectral shift. A possible explanation is the nature of D2 which is ascribed to the complex coupling, interference and spectral superposition between the propagating surface plasmons associated with the grating resonances related to the periodic nanostructure arrangement and the localized resonances confined at the individual sharp grating tips decorated with nanoscale grooves. As such, the D2 trough is more sensitive

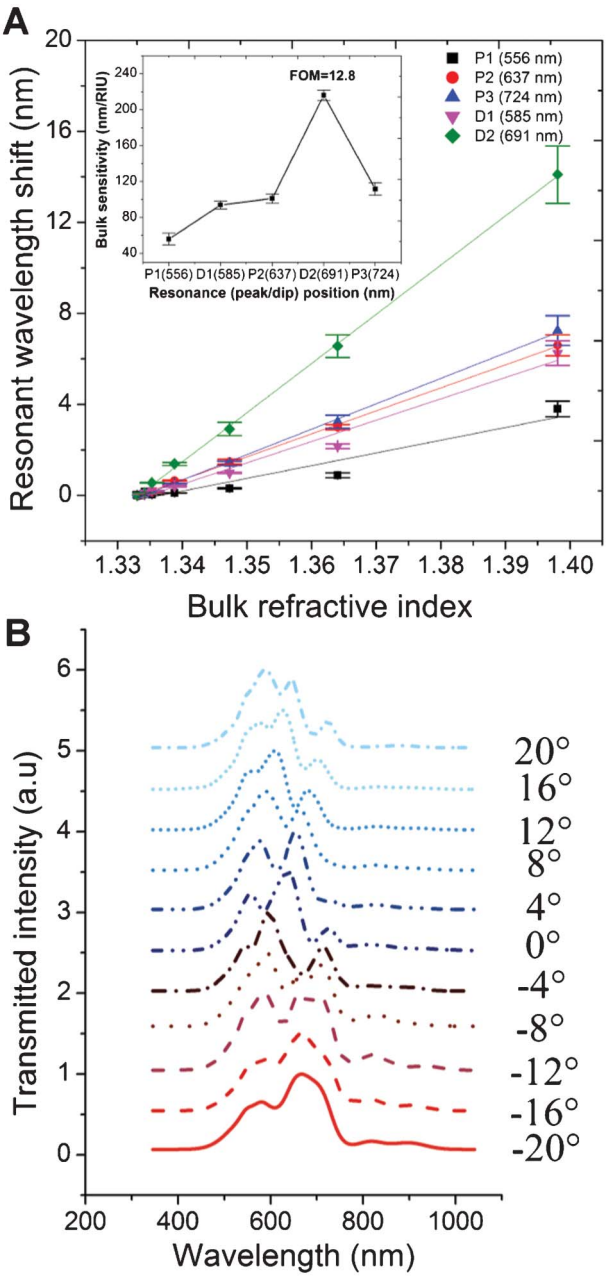

Fig. 3 (a) Resonant wavelength shift for different bulk refractive indices at normal incidence. The inset shows the sensitivity for different resonant wavelengths with the corresponding figure of merit (FOM) for the most sensitive resonance. (b) Transmitted intensity of p-polarized light through a 50 nm thick gold film on the blazed grating for angle of incidence $\theta = -20°, -16°, \ldots, -4°, 0°, 4°, \ldots, 16°, 20°$. The curves have been normalized to 1 and offset for clarity.

than the neighbouring peaks because it captures the coupling resonance between the propagating and localized fields at the sharp corners of the gold film and as such also includes the spectral movement in both P2 and P3.

In order to investigate the possible sensitivity enhancement, in addition to normal incidence, we also performed transmission measurements at different incident angles (from −20° to 20° in 4° increments). The corresponding transmission spectra

for a bulk refractive index of 1.333 are shown in Fig. 3b. By changing the incident angle we demonstrated the ability to tune the resonant wavelength of the sensor. This feature can be explored to enhance the sensitivity by increasing the asymmetry of ± 1 orders' strengths, resulting in the highly asymmetric excitation of SPPs on the blazed gratings. The sensitivity of the device as a function of the incident angle was obtained by varying the bulk refractive index, recording the transmission spectra (see Fig. S3, ESI†) and extracting the wavelength shift for each resonance (see Fig. S4, ESI†). In Fig. 4a we show the resonance shift of the first minimum in the spectrum for which we obtained a maximum sensitivity of 773 nm/RIU with a FOM of 55.2/RIU at a rotational angle of 12° (Fig. 4b). This sensitivity is higher than the previously reported data for regular arrays of nanoslits[39] (427 nm/RIU), nanoholes[35] (470 nm/RIU) and grove-slit nanointerferometers[90](630 nm/RIU).

T-SPR kinetic measurements

While the maximum sensitivity for the blazed gratings occurred at an angle of 12°, stringent angular control and alignment is difficult in integrated optical devices suitable for POC diagnosis which is why normal incidence was chosen for all the kinetic binding experiments. Herein, we measured each peak/dip wavelength shift for different surface binding reactions, as shown in Fig. 5. Following the surface functionalization with thiolated PEG-Biotin (Fig. 5a), a 1 μg mL^{-1} streptavidin concentration was flowed through the microfluidic chamber and the corresponding binding curves are shown in Fig. 5b. From the obtained results, we determined that for the binding interactions, the maximum resonant wavelength shift, $\Delta\lambda_{max}$ (maximum sensitivity) occurred for the resonance around 690 nm (first minimum in the transmission spectrum), which corresponds to the results obtained for the bulk refractive index change. This was also confirmed for the anti CD44 antibody immobilization on the grating surface, as shown in Fig. 5c. By comparing the binding kinetics in Fig. 5, it is interesting to note that each peak responded differently to a specific binding event. In particular, the observed sensitivity splitting in Fig. 5b between peaks 2 and 3 could be related to the nonlinear target dependent sensitivity of our sensor which was previously observed with other nanostructured SPR systems.[17,91,92] Additionally, the inhomogeneous nature of the target binding to the surface affected each resonance differently due to the complex interplay between SPPs, LSPs and their interactions. In each case, however, $\Delta\lambda_{max}$ was obtained for the second minimum of the transmission curve which closely corresponded to the sum of the shifts in the neighbouring peaks, further suggesting the spectral superposition between the SPPs associated with the grating resonances related to the periodic nanostructure arrangement and the localized resonances confined at the individual sharp grating tips with nanoscale grooves. Therefore, for the subsequent antibody–antigen binding study, only this resonance was extracted and used to obtain sandwich immunoassay kinetic curves.

Following antibody immobilization, we performed quantitative kinetic sandwich immunoassay measurements by sequentially introducing different concentrations of CD44 antigen (or control) into the eight microfluidic chambers. Following CD44 binding, a secondary detection antibody, anti-CD44 (dAb), was used to amplify the detection signal. CD44 was chosen as a model protein for our sensing experiments and device characterization due to its involvement in the progression of human malignant tumors and metastasis formation[93–96] and its potential as a clinical cancer biomarker. In the majority of human tumors, overexpression of CD44 characterizes tumor progression and dissemination.[97–100] In addition to cell surface expression, substantial amounts of sCD44 generated either by shedding or alternative splicing can be found in physiological fluids. The increased levels of sCD44

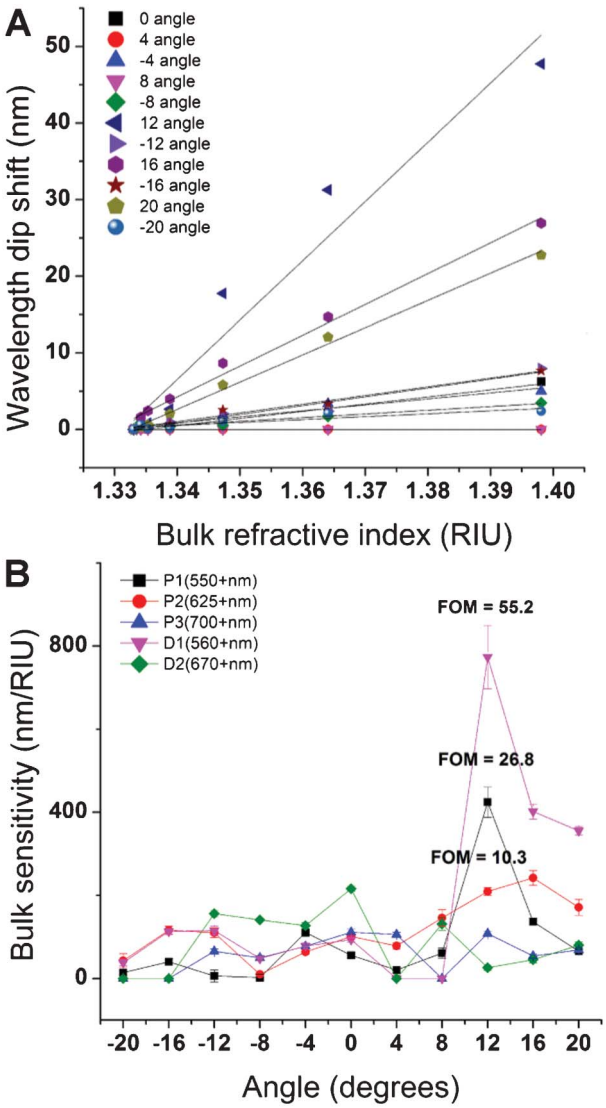

Fig. 4 (a) Wavelength shift as a function of the sample rotational angle (incidence angle) for the resonant wavelength corresponding to the first minimum in the transmitted spectrum (symbols represent the experimental data and the line is a best fit using linear regression). Zero points correspond to the polarizations where the SPRs are not excited and thus no fit could be performed. (b) The sensitivity of the blazed grating as a function of the incident angle taken as a linear regression slope for the refractive index dependence at each resonant wavelength in Fig. S4 (a–e).†

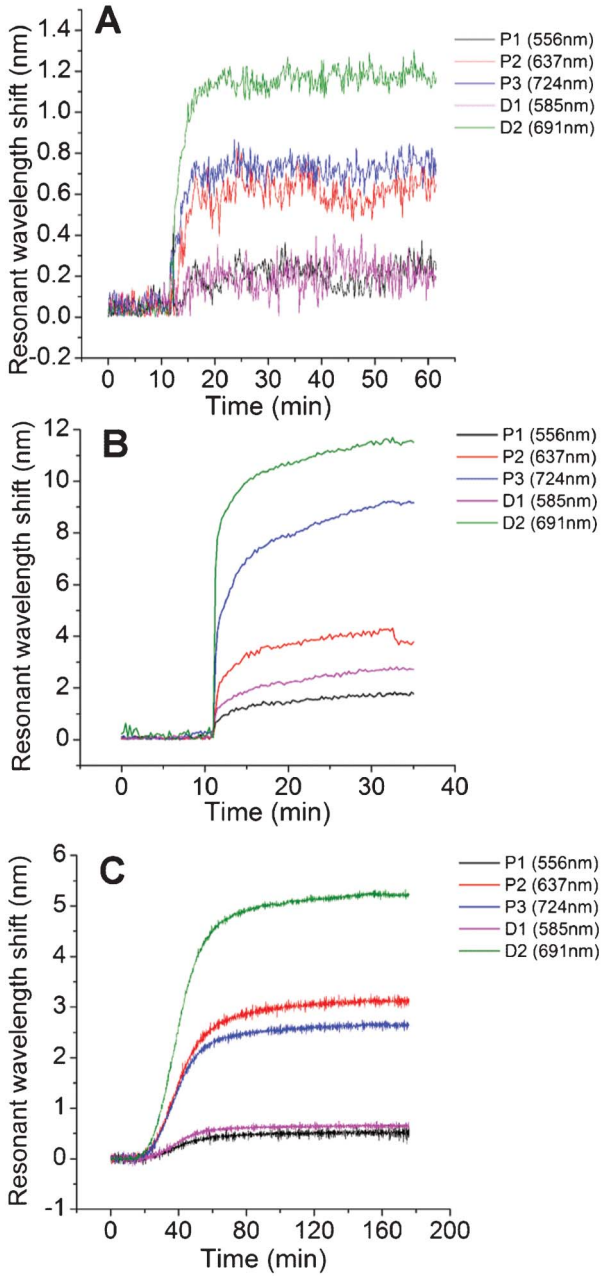

Fig. 5 Average of five kinetic curves for each resonant peak representing (a) thiolated PEG-biotin surface functionalization, (b) 1 μg mL^{-1} streptavidin binding to the functionalized surface and (c) capture antibody immobilization onto the carboxyl activated surface.

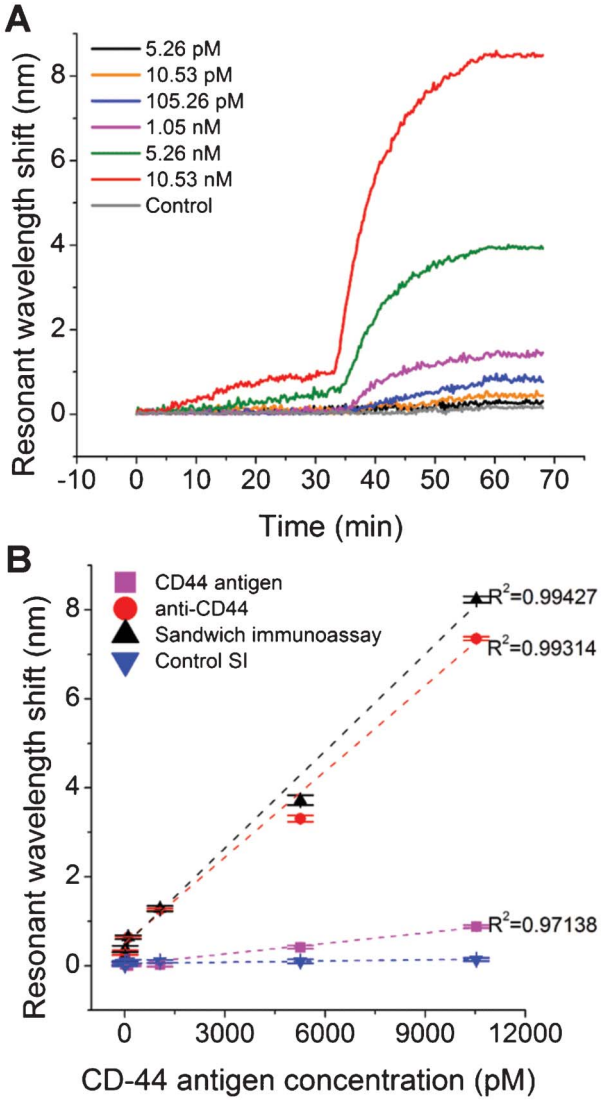

Fig. 6 Kinetic curves of CD44 binding to the surface for (a) different peaks; (b) at maximum peak for different concentrations (binding constants for anti-CD44 binding to the bound CD44 are k_{on} = 7.14 ± 0.32 × 10^6 M^{-1} min^{-1}; k_{off} = 7.43 ± 0.30 × 10^{-2} min^{-1}; the affinity k_d is 1.041 ± 0.08 × 10^{-8} M).

during inflammation and in cancer patients, range from ~250 pM in saliva[3,101] to ~10 nM in serum,[102,103] compared to the lower physiological sCD44 level in healthy people (10 pM to 5 nM, respectively).[2,104–106] Therefore, the CD44 concentration range used in this study corresponded to clinically relevant concentrations from 5 pM up to 10 nM (Fig. 6). From Fig. 6a, the minimum detectable CD44 concentration without the secondary antibody amplification step corresponded to 5.26 nM, while the limit of detection was decreased to 10.53 pM using a secondary dAb in a sandwich immunoassay format. The binding constants for the anti-CD44 dAb binding to the captured CD44 were estimated to be k_a = 7.14 ± 0.32 × 10^6 M^{-1} min^{-1}; k_d = 7.43 ± 0.30 × 10^{-2} min^{-1}; and the affinity K_D = 1.041 ± 0.08 × 10^{-8} M. Fig. 6b shows the plot of the total resonance wavelength shift as a function of the CD44 antigen concentration. A good linear fit of the experimentally obtained data points was obtained for the sandwich immunoassay format (Fig. 6b), suggesting the possibility to use the device for a wide range of targets in bioanalytical research. It is noteworthy that the presented optical system, used for NMF device characterization, relied on a fiber-based spectrometer, which limited the biosensor throughput to sequential measurements. To overcome this limitation, we are developing a setup that employs a CCD camera which would allow multiplexed SPR imaging spectroscopy to fully exploit the high throughput offered by the multichannel device.

Conclusions

We reported the design, fabrication and characterization of a novel nanoplasmonic microfluidic (NMF) biosensor that integrates in a single monolithic polymer substrate both a nanostructured surface required for plasmonic response monitoring and a network of microchannels for precise flow control. A novel technique for rapid, low-cost fabrication of molds containing large-area nanostructures and easily interchangeable microfluidic channel layouts was developed.[75] The resulting 3D hierarchical molds enabled the fabrication of NMF devices using a low-cost mass-production compatible process that is industrially viable. Additionally, the monolithic integration of nanoplasmonic elements within the flow layer allowed the use of an active top cover containing multiple pneumatic valve elements in thermoplastics. To the best of our knowledge, this is the first demonstration integrating thermoplastic valves in such a large number, opening the possibility for individual row/column addressing in a multiplex detection scheme. The fabricated NMF biosensor was employed for the quantitative detection of protein binding interactions at clinically relevant concentrations using a label-free enhanced transmission surface plasmon resonance technique. Compared to recently reported nanoslit or nanohole arrays, the proposed sensor exhibited $\sim$50% higher wavelength sensitivity under an optimized incidence angle (773 nm/RIU), reaching a figure of merit of up to 55/RIU. The obtained results suggest that the system presented here is a promising approach for the development of high-throughput, compact biosensors amenable to large scale, on-chip integration that are capable of satisfying the reliability, affordability, and portability requirements for POC applications. Future work is directed towards integrating the multichannel device with spectral SPR imaging using a small CCD spectrometer for a portable POC system.

Acknowledgements

The authors thank the Genome-Quebec and the National Research Council of Canada for their financial support. We also thank Daniel Brassard for his expertise and help with the fabrication of thermoplastic elastomer membranes.

References

1 D. W. G. Morrison, M. R. Dokmeci, U. Demirci and A. Khademhosseini, *Clinical Applications of Micro- and Nanoscale Biosensors*, Wiley, 2007.
2 T. Päll, A. Pink, L. Kasak, M. Turkina, W. Anderson, A. Valkna and P. Kogerman, *PLoS One*, 2011, **6**, e29305.
3 E. J. Franzmann, E. P. Reategui, F. Pedroso, F. G. Pernas, B. M. Karakullukcu, K. L. Carraway, K. Hamilton, R. Singal and W. J. Goodwin, *Cancer Epidemiol., Biomarkers Prev.*, 2007, **16**, 1348–1355.
4 D. A. Giljohann and C. A. Mirkin, *Nature*, 2009, **462**, 461–464.
5 A. Rasooly and J. Jacobson, *Biosens. Bioelectron.*, 2006, **21**, 1851–1858.
6 J. Homola, *Surface Plasmon Resonance Based Sensors*, Springer, Heidelberg, 2006.
7 J. N. Anker, W. P. Hall, O. Lyandres, N. C. Shah, J. Zhao and R. P. Van Duyne, *Nat. Mater.*, 2008, **7**, 442–453.
8 K. L. Kelly, E. Coronado, L. L. Zhao and G. C. Schatz, *J. Phys. Chem. B*, 2002, **107**, 668–677.
9 G. McNay, D. Eustace, W. E. Smith, K. Faulds and D. Graham, *Appl. Spectrosc.*, 2011, **65**, 825–837.
10 B. H. Jun, G. Kim, M. S. Noh, H. Kang, Y. K. Kim, M. H. Cho, D. H. Jeong and Y. S. Lee, *Nanomedicine*, 2011, **6**, 1463–1480.
11 K. W. Kho, C. Y. Fu, U. S. Dinish and M. Olivo, *J. Biophotonics*, 2011, **4**, 667–684.
12 K. Kim and K. S. Shin, *Anal. Sci.*, 2011, **27**, 775–783.
13 Y. Zhang, H. Hong, D. V. Myklejord and W. Cai, *Small*, 2011, **7**, 3261–3269.
14 S. J. Chen, F. C. Chien, G. Y. Lin and K. C. Lee, *Opt. Lett.*, 2004, **29**, 1390–1392.
15 L. Malic, B. Cui, T. Veres and M. Tabrizian, *Opt. Lett.*, 2007, **32**, 3092–3094.
16 K. M. Byun, S. J. Yoon, D. Kim and S. J. Kim, *Opt. Lett.*, 2007, **32**, 1902–1904.
17 L. Malic, B. Cui, M. Tabrizian and T. Veres, *Opt. Express*, 2009, **17**, 20386–20392.
18 K. Byun, S. Kim and D. Kim, *Opt. Express*, 2005, **13**, 3737–3742.
19 K. M. Byun, D. Kim and S. J. Kim, *Sens. Actuators, B*, 2006, **117**, 401–407.
20 D. Kim, *J. Opt. Soc. Am. A*, 2006, **23**, 2307–2314.
21 K. Kim, S. J. Yoon and D. Kim, *Opt. Express*, 2006, **14**, 12419–12431.
22 J. Zhao, X. Zhang, C. Yonzon, A. J. Haes and R. P. V. Duyne, *Nanomedicine*, 2006, **1**, 219–228.
23 C. L. Haynes and R. P. Van Duyne, *J. Phys. Chem. B*, 2001, **105**, 5599–5611.
24 A. Haes and R. Duyne, *Anal. Bioanal. Chem.*, 2004, **379**, 920–930.
25 A. J. Haes, C. L. Haynes, A. D. McFarland, S. Zou, G. C. Schatz and R. P. V. Duyne, *MRS Bull.*, 2005, **30**, 368–375.
26 D. A. Stuart, A. J. Haes, C. R. Yonzon, E. M. Hicks and R. P. V. Duyne, *IEE Proc.: Nanobiotechnol.*, 2005, **152**, 13–32.
27 M. Svedendahl, S. Chen, A. Dmitriev and M. Käll, *Nano Lett.*, 2009, **9**, 4428–4433.
28 S. J. Zalyubovskiy, M. Bogdanova, A. Deinega, Y. Lozovik, A. D. Pris, K. H. An, W. P. Hall and R. A. Potyrailo, *J. Opt. Soc. Am. A*, 2012, **29**, 994–1002.
29 V. Canpean and S. Astilean, *Lab Chip*, 2009, **9**, 3574–3579.
30 A. Degiron and T. W. Ebbesen, *J. Opt. A: Pure Appl. Opt.*, 2005, **7**, S90.
31 F. Eftekhari, C. Escobedo, J. Ferreira, X. Duan, E. M. Girotto, A. G. Brolo, R. Gordon and D. Sinton, *Anal. Chem.*, 2009, **81**, 4308–4311.
32 R. Gordon, D. Sinton, K. L. Kavanagh and A. G. Brolo, *Acc. Chem. Res.*, 2008, **41**, 1049–1057.
33 J. F. Masson, M. P. Murray-Methot and L. S. Live, *Analyst*, 2010, **135**, 1483–1489.
34 P. R. Stark, A. E. Halleck and D. N. Larson, *Methods*, 2005, **37**, 37–47.

35 S. H. Lee, N. Lindquist, N. J. Wittenberg, L. R. Jordan and S.-H. Oh, *Lab Chip*, 2012, **12**, 3882–3890.
36 N. C. Lindquist, A. Lesuffleur, H. Im and S.-H. Oh, *Lab Chip*, 2009, **9**, 382–387.
37 A. A. Yanik, M. Huang, O. Kamohara, A. Artar, T. W. Geisbert, J. H. Connor and H. Altug, *Nano Lett.*, 2010, **10**, 4962–4969.
38 A. Cattoni, P. Ghenuche, A.-M. Haghiri-Gosnet, D. Decanini, J. Chen, J.-L. Pelouard and S. P. Collin, *Nano Lett.*, 2011, **11**, 3557–3563.
39 K.-L. Lee, P.-W. Chen, S.-H. Wu, J.-B. Huang, S.-Y. Yang and P.-K. Wei, *ACS Nano*, 2012, **6**, 2931–2939.
40 J. Guo and H. Leong, *J. Opt. Soc. Am. B*, 2012, **29**, 1712–1716.
41 Y. S. Jung, Z. Sun, J. Wuenschell, H. K. Kim, P. Kaur, L. Wang and D. Waldeck, *Appl. Phys. Lett.*, 2006, **88**, 243105–243103.
42 A. Karabchevsky, O. Krasnykov, I. Abdulhalim, B. Hadad, A. Goldner, M. Auslender and S. Hava, *Photonics Nanostruct.*, 2009, **7**, 170–175.
43 K.-L. Lee and P.-K. Wei, *Appl. Phys. Lett.*, 2011, **99**, 083108.
44 B. K. Singh and A. C. Hillier, *Anal. Chem.*, 2008, **80**, 3803–3810.
45 W.-H. Yeh, J. W. Petefish and A. C. Hillier, *Anal. Chem.*, 2011, **83**, 6047–6053.
46 W.-H. Yeh, J. Kleingartner and A. C. Hillier, *Anal. Chem.*, 2010, **82**, 4988–4993.
47 Z.-C. Xu, B. Dong, B.-R. Lu, Y. Chen, E. Huq, X.-P. Qu and R. Liu, *Microelectron. Eng.*, 2011, **88**, 2647–2649.
48 K. M. Byun, S. J. Kim and D. Kim, *Appl. Opt.*, 2007, **46**, 5703–5708.
49 J. Dostálek, J. Homola and M. Miler, *Sens. Actuators, B*, 2005, **107**, 154–161.
50 J. Homola, *Chem. Rev.*, 2008, **108**, 462–493.
51 D. G. Myszka, X. He, M. Dembo, T. A. Morton and B. Goldstein, *Biophys. J.*, 1998, **75**, 583–594.
52 J. Ozhikandathil, S. Badilescu and M. Packirisamy, *J. Biomed. Opt.*, 2012, **17**, 077001.
53 S. Y. Lee, S.-H. Kim, S. G. Jang, C.-J. Heo, J. W. Shim and S.-M. Yang, *Anal. Chem.*, 2011, **83**, 9174–9180.
54 A. Prabhakar and S. Mukherji, *Lab Chip*, 2010, **10**, 3422–3425.
55 Y. Zhang, Y. Tang, Y.-H. Hsieh, C.-Y. Hsu, J. Xi, K.-J. Lin and X. Jiang, *Lab Chip*, 2012, **12**, 3012–3015.
56 J. C. Sharpe, J. S. Mitchell, L. Lin, N. Sedoglavich and R. J. Blaikie, *Anal. Chem.*, 2008, **80**, 2244–2249.
57 J. Ji, J. G. O'Connell, D. J. D. Carter and D. N. Larson, *Anal. Chem.*, 2008, **80**, 2491–2498.
58 A. De Leebeeck, L. K. S. Kumar, V. de Lange, D. Sinton, R. Gordon and A. G. Brolo, *Anal. Chem.*, 2007, **79**, 4094–4100.
59 A. Lesuffleur, H. Im, N. C. Lindquist, K. S. Lim and S.-H. Oh, *Opt. Express*, 2008, **16**, 219–224.
60 L. Guo, Y. Yin, R. Huang, B. Qiu, Z. Lin, H. H. Yang, J. Li and G. N. Chen, *Lab Chip*, 2012, **12**, 3901–3906.
61 A. A. Yanik, M. Huang, A. Artar, T.-Y. Chang and H. Altug, *Appl. Phys. Lett.*, 2010, **96**, 021101.
62 C. Escobedo, A. G. Brolo, R. Gordon and D. Sinton, *Nano Lett.*, 2012, **12**, 1592–1596.
63 F. Rohde and R. Porcar, BioPhotonics, 2011 International workshop on, 2011, 1–3.
64 C. Huang, K. Bonroy, G. Reekmans, W. Laureyn, K. Verhaegen, I. De Vlaminck, L. Lagae and G. Borghs, *Biomed. Microdevices*, 2009, **11**, 893–901.
65 H. Chengjun, J. Putzeys, Y. Jian, G. Reekmans, K. Verhaegen, L. Lagae, K. Verstreken and G. Borghs, Sensors Applications Symposium, 2009, SAS 2009, IEEE, 2009, 43–46.
66 C. Huang, J. Ye, S. Wang, T. Stakenborg and L. Lagae, *Appl. Phys. Lett.*, 2012, **100**, 173114.
67 T. Glinsner, T. Veres, G. Kreindl, E. Roy, K. Morton, T. Wieser, C. Thanner, D. Treiblmayr, R. Miller and P. Lindner, *Microelectron. Eng.*, 2010, **87**, 1037–1040.
68 D. Brassard, L. Clime, K. Li, M. Geissler, C. Miville-Godin, E. Roy and T. Veres, *Lab Chip*, 2011, **11**, 4099–4107.
69 L. Zhou, F. Ding, H. Chen, W. Ding, W. Zhang and S. Y. Chou, *Anal. Chem.*, 2012, **84**, 4489–4495.
70 E. Roy, J.-C. Galas and T. Veres, *Lab Chip*, 2011, **11**, 3193–3196.
71 L. Malic, B. Cui, T. Veres and M. Tabrizian, *Opt. Lett.*, 2007, **32**, 3092–3094.
72 S. Park, G. Lee, S. H. Song, C. H. Oh and P. S. Kim, *Opt. Lett.*, 2003, **28**, 1870–1872.
73 J. B. Lassiter, H. Sobhani, J. A. Fan, J. Kundu, F. Capasso, P. Nordlander and N. J. Halas, *Nano Lett.*, 2010, **10**, 3184–3189.
74 L. Malic, M. G. Sandros and M. Tabrizian, *Anal. Chem.*, 2011, **83**, 5222–5229.
75 L. Malic, K. Morton, L. Clime and T. Veres, *International Patent Application*, 2012, p. WO 2012/122628.
76 N. Bonod, E. Popov, L. Li and B. Chernov, *Opt. Express*, 2007, **15**, 11427–11432.
77 B. Bai, X. Meng, J. Laukkanen, T. Sfez, L. Yu, W. Nakagawa, H. P. Herzig, L. Li and J. Turunen, *Phys. Rev. B: Condens. Matter Mater. Phys.*, 2009, **80**, 035407.
78 F. Lopez-Tejeira, S. G. Rodrigo, L. Martin-Moreno, F. J. Garcia-Vidal, E. Devaux, T. W. Ebbesen, J. R. Krenn, I. P. Radko, S. I. Bozhevolnyi, M. U. Gonzalez, J. C. Weeber and A. Dereux, *Nat. Phys.*, 2007, **3**, 324–328.
79 N. P. Wanstall, T. W. Preist, W. C. Tan, M. B. Sobnack and J. R. Sambles, *J. Opt. Soc. Am. A*, 1998, **15**, 2869–2876.
80 V. I. Belotelov, A. N. Kalish, A. K. Zvezdin, A. V. Gopal and A. S. Vengurlekar, *J. Opt. Soc. Am. B*, 2012, **29**, 294–299.
81 B. Luk'yanchuk, N. I. Zheludev, S. A. Maier, N. J. Halas, P. Nordlander, H. Giessen and C. T. Chong, *Nat. Mater.*, 2010, **9**, 707–715.
82 P. B. Johnson and R. W. Christy, *Phys. Rev. B: Solid State*, 1972, **6**, 4370–4379.
83 S. H. Choi, S. J. Kim and K. M. Byun, *Opt. Commun.*, 2010, **283**, 2961–2966.
84 C. Genet and T. W. Ebbesen, *Nature*, 2007, **445**, 39–46.
85 J. Homola, *Surface Plasmon Resonance Based Sensors*, Springer-Verlag Berlin Heidelberg, New York, 2006.
86 K.-L. Lee, W.-S. Wang and P.-K. Wei, *Plasmonics*, 2008, **3**, 119–125.
87 S. K. Dondapati, T. K. Sau, C. Hrelescu, T. A. Klar, F. D. Stefani and J. Feldmann, *ACS Nano*, 2010, **4**, 6318–6322.
88 G. J. Nusz, S. M. Marinakos, A. C. Curry, A. Dahlin, F. Hook, A. Wax and A. Chilkoti, *Anal. Chem.*, 2008, **80**, 984–989.

89 G. J. Nusz, A. C. Curry, S. M. Marinakos, A. Wax and A. Chilkoti, *ACS Nano*, 2009, **3**, 795–806.
90 J. Feng, V. S. Siu, A. Roelke, V. Mehta, S. Y. Rhieu, G. T. R. Palmore and D. Pacifici, *Nano Lett.*, 2011, **12**, 602–609.
91 S. J. Yoon and D. Kim, *J. Opt. Soc. Am. A*, 2008, **25**, 725–735.
92 K. M. Byun, S. M. Jang, S. J. Kim and D. Kim, *J. Opt. Soc. Am. A*, 2009, **26**, 1027–1034.
93 S. Jothy, *Clin. Exp. Metastasis*, 2003, **20**, 195–201.
94 S. Lee, K. Lee, H. Chang, M. Choi, M.-S. Cho, S. Min, H. Lee, Y. Mun, E. Nam, C. Seong and S. Lee, *Ann. Surg. Oncol.*, 2008, **15**, 1155–1160.
95 U. Valentiner, F. U. Valentiner and U. Schumacher, *Tumor Biol.*, 2008, **29**, 152–160.
96 R. Marhaba and M. Zöller, *J. Mol. Histol.*, 2004, **35**, 211–231.
97 K. Zen, D.-Q. Liu, Y.-L. Guo, C. Wang, J. Shan, M. Fang, C.-Y. Zhang and Y. Liu, *PLoS One*, 2008, **3**, e1826.
98 Q.-T. Le, E. Chen, A. Salim, H. Cao, C. S. Kong, R. Whyte, J. Donington, W. Cannon, H. Wakelee, R. Tibshirani, J. D. Mitchell, D. Richardson, K. J. O'Byrne, A. C. Koong and A. J. Giaccia, *Clin. Cancer Res.*, 2006, **12**, 1507–1514.
99 O. Watanabe, J. Kinoshita, T. Shimizu, H. Imamura, A. Hirano, T. Okabe, M. Aiba and K. Ogawa, *J. Exp. Clin. Cancer Res.*, 2005, **24**, 75–82.
100 H. N. Zavrides, A. Zizi-Sermpetzoglou, D. Panousopoulos, G. Athanasas, I. Elemenoglou and G. Peros, *Folia Histochem. Cytobiol.*, 2005, **43**, 31–36.
101 E. J. Franzmann, E. P. Reategui, K. L. Carraway, K. L. Hamilton, D. T. Weed and W. J. Goodwin, *Cancer Epidemiol., Biomarkers Prev.*, 2005, **14**, 735–739.
102 Y.-J. Guo, G. Liu, X. Wang, D. Jin, M. Wu, J. Ma and M.-S. Sy, *Cancer Res.*, 1994, **54**, 422–426.
103 S. Molica, G. Vitelli, D. Levato, D. Giannarelli and G. M. Gandolfo, *Cancer*, 2001, **92**, 713–719.
104 S. Mayer, A. zur Hausen, D. O. Watermann, S. Stamm, M. Jager, G. Gitsch and E. Stickeler, *J. Cancer Res. Clin. Oncol.*, 2008, **134**, 1229–1235.
105 N. Niitsu and K. Iijima, *Leuk. Res.*, 2002, **26**, 241–248.
106 H. Máenpáá, R. Ristamáki, J. Virtamo, K. Franssila, D. Albanes and H. Joensuu, *Leuk. Lymphoma*, 2000, **37**, 585–592.